Journal of Materials Chemistry A

Low-Temperature Sprayed SnO_x Nanocomposite Films with Enhanced Hole Blocking for Efficient Large Area Perovskite Solar Cells

Journal:	*Journal of Materials Chemistry A*
Manuscript ID	TA-ART-07-2021-005969.R1
Article Type:	Paper
Date Submitted by the Author:	24-Aug-2021
Complete List of Authors:	Zhang, Jinbao; Xiamen University, Materials Ding, Yichuan; Stanford University, Material Science and Engineering Jiang, Guochen; Tsinghua University Flick, Austin; Stanford University, Materials Science and Engineering Pan, Ziyi; Stanford University, Chemistry Scheideler, William; Dartmouth College, Thayer School of Engineering Zhao, Oliver; Stanford University Chen, Justin; Stanford University, Materials Science and Engineering; Yang, Li; Xiamen University Rolston, Nicholas; Stanford University, Applied Physics Dauskardt, Reinhold; Stanford University, Materials Science and Engineering

Low-Temperature Sprayed SnO_x Nanocomposite Films with Enhanced Hole Blocking for Efficient Large Area Perovskite Solar Cells

*Jinbao Zhang,[a,d] Yichuan Ding,[a] Guochen Jiang,[a,e] Austin C. Flick,[a] Ziyi Pan,[b] William J. Scheideler,[a,f] Oliver Zhao,[a] Justin P. Chen,[a] Li Yang,[d] Nicholas Rolston, [c] Reinhold H. Dauskardt [a]**

[a] Department of Materials Science and Engineering
Stanford University, Stanford, CA 94305-2205, United States
E-mail: rhd@stanford.edu

[b] Department of Chemistry
Stanford University, Stanford, CA 94305-2205, United States

[c] Department of Applied Physics
Stanford University, Stanford, CA 94305-2205, United States

[d] Now at Department of Materials, Fujian Key Laboratory of Advanced Materials, Xiamen University, Xiamen, 361005, Fujian, China

[e] Now at School of Materials Science and Engineering
Tsinghua University, Beijing, 100084, P. R. China

[f] Now at School of Engineering
Dartmouth University, Hanover, NH

Keywords: spray coating, SnO_2 nanocomposite, ambient processing, perovskite solar modules

Abstract

Scalable fabrication of charge transport layers with high uniformity and compactness is essential for the commercialization of perovskite solar cells (PSCs). Cost-effective deposition of high-quality electron transport layers (ETLs) is a particularly important step to achieve low-cost, efficient and large-area PSCs. Here, an open-air (relative humidity of 40-50%) and low-temperature ($\leqslant 100^{o}C$) ultrasonic spray coating of tin oxide (SnO_2) nanocomposite films incorporating nanocrystalline SnO_2 nanoparticles in an amorphous SnO_x matrix is demonstrated to fabricate large-area ETLs for planar PSCs. The optimized SnO_2/SnO_x nanocomposite exhibits significantly enhanced hole-blocking and high-power conversion efficiencies of 18% and 16% for planar PSCs with active area of 0.2 cm^2 and 1 cm^2, respectively. More importantly, the devices show little current-voltage hysteresis as well as good shelf-life stability by maintaining ~90% of initial performance without encapsulation after 2500 hours storage under inert conditions. Furthermore, high voltages of >6.0 V have been obtained for solar modules of 2.1 cm^2 aperture area comprising six sub-cells in series, suggesting that the low-temperature, open-air and fast spray coating is suitable and transferable to deposit large-area charge transport layers for scalable PSCs or other optoelectronic devices.

Introduction

Organic-inorganic hybrid perovskite semiconductors (e.g. $CH_3NH_3PbI_3$) have demonstrated potential for solar cell applications owing to their outstanding optoelectronic properties and ease of manufacturing.[1] Both power conversion efficiencies (PCEs) and stability of perovskite solar cells (PSCs) have recently shown significant improvements as a result of efforts in materials engineering as well as device optimization.[2,3,4] Scalable and low-cost fabrication of functional layers in PSCs has now become the major challenge for the commercialization of PSC technology.[5]

Regarding device architecture, planar structured PSCs have received more attention compared to mesoporous ones due to a simpler fabrication process and lower thermal budget.[6] Planar PSCs have a simple sandwich structure with an electron transport layer (ETL) and hole transport layer (HTL) located on either side of the perovskite light absorber for collecting photoinduced charges. In terms of planar PSCs scalability, great efforts have been devoted to developing new deposition methods for large-area perovskite thin films, such as atmospheric plasma spray,[7] vacuum flash assisted process,[8] spray coating,[9] blade coating,[10] slot die coating,[11] and ink drying[12]. Recent developments in scaling of the perovskite absorber layer are described elsewhere.[13,14]

Techniques for scalable fabrication of charge transport layers are equally important. HTLs from organic materials show high structural versatility[15,16] and can be deposited in large areas by thermal evaporation.[17] However, state-of-the-art ETL deposition still relies on non-scalable processes like spin coating, especially for metal oxide ETLs. In spin coating, a high-concentration precursor is necessary to achieve a full coverage film over the substrate and is only suitable for small substrates. Moreover, spin-coating has a low conversion yield and is not appropriate for large scale solar cell fabrication or readily adaptable to flexible substrates. Therefore, there is motivation to develop a scalable and cost-effective deposition method for ETLs that can also be applied to flexible form factors.

In n-i-p PSCs, the ETL is one of the most important components related to solar cell efficiency. It is necessary for an efficient ETL to have high transparency in visible light, an appropriate work function for electrical conductivity, high radiative stability, and good chemical compatibility with the perovskite layer.[18] To date, the most efficient and reliable ETLs in PSCs are made from inorganic metal oxides, e.g. TiO_2,[19] SnO_2,[20] or ZnO.[21] However, such metal-oxides-based ETLs pose challenges for scalable fabrication, because 1) they typically require high-temperature annealing to increase conductivity, 2) they generally have a high boiling point, making deposition by thermal evaporation difficult, and 3) it is challenging to obtain smooth and pinhole free metal oxides layers by a single-pass deposition as compared to their organic counterparts.

SnO_2 has recently been identified as one of the most promising ETL candidates for PSCs because of its faster interfacial charge extraction, higher electron mobility as well as better stability under ultraviolet illumination compared to conventional TiO_2 [22] and improved thermal stability compared to ZnO.[23] Another advantage of SnO_2 is its amenability to low-temperature deposition, which is favorable for flexible, lightweight device applications.

In order to obtain high-quality SnO_2 ETLs, different strategies have been reported to optimize morphology, composition and crystallinity for achieving high PCEs over 20% for small cells, including spin coating of colloidal SnO_2,[24] vapor deposition,[25] and sol-gel synthesis.[26] Meanwhile, preliminary attempts have been made to scale the SnO_2 ETL layers in PSCs. For example, slot-die printed SnO_2 nanoparticles have been used in flexible PSCs along with an effective passivation strategy to achieve a high PCE of about 15% for large area PSCs.[18] Another study utilized room-temperature sputtered SnO_2 enabling PCEs over 12% for large-area cells.[27] However, these approaches usually require additional surface passivation, high temperature (>180^{o}C) annealing, or sophisticated deposition processes involving large capital expenditure.[28]

Considering these challenges, we applied an effective strategy to produce a SnO_2/SnO_x nanocomposite incorporating sprayed SnO_2 nanoparticle and sol-gel of

$SnCl_2$. Spray coating is an excellent method for large-area thin film fabrication through solution processes, in which spraying parameters such as viscosity, flow of solution, and substrate temperature need to be carefully optimized in order to obtain high quality films.[28] Previously, our research group has successfully demonstrated the use of open-air spray coating for perovskite solar cells to fabricate large-area perovskite thin films,[7] barrier layers,[30] and NiO HTLs.[31]

Electrochemical cyclic voltammetry characterization was used to demonstrate that the resulting sprayed nanocomposite structure increased the hole blocking effectiveness and thus reduced the interfacial charge recombination loss contributing to significantly enhanced open circuit voltage (V_{oc}) in solar cells by 16% increase (>100 mV). The sprayed SnO_2 nanocomposite ETL in planar PSCs in the present study enabled a high PCE of over 18% with negligible hysteresis. Finally, an all-sprayed SnO_2 nanocomposite was successfully used to fabricate large-area devices (>1 cm^2) and solar modules (6 cells in series with active area of 2.1 cm^2).

Results and Discussion

1. Optimization of SnO_2 nanoparticles spray parameters

The sprayed thin film quality was sensitive to the deposition conditions and a spray parameter optimization was initially performed. The as-purchased SnO_2 colloidal solution (15 wt%) was diluted in H_2O to reach 0.1 wt%, followed by a 15-minute sonication. A programmable spray nozzle was used for spraying SnO_2 onto ITO substrates (2 x 2 cm^2) placed on a hotplate, as illustrated in Figure 1a. The spray head was scanned at a speed of 25 mm/s in a serpentine pattern with 2 mm spacing. According to our previous experience in spray coating NiO,[7] the optimal distance between nozzle and the substrate was fixed at 8 cm and N_2 carrier gas pressure kept constant at 2 liters per minute (LPM).

We studied the influence of three important variables (substrate temperature, flow rate of precursor and solvents) on the quality of SnO_2 films. Firstly, we studied the effect of substrate temperature from 25˚C to 200˚C. As shown in Figure S1a, a significant

"coffee-ring effect" was observed for room temperature sprayed films,[32] which is due to the capillary flow induced by different solvent evaporation rates across the droplets, where the faster evaporation of the solvent at the droplet edges is replenished by the interior solution. As illustrated in Figure S6, the resulting liquid flow can transport SnO_2 nanoparticles from the droplet center to the edge producing unwanted coffee rings.

With increased substrate temperature to 80˚C - 100˚C (Figure S1), the coffee-ring features decreased and the film became smoother, indicating temperature control is an effective way to improve film quality.[18,33] Solvent evaporation was faster at the higher substrate temperatures significantly shortening the flow time and reducing the accumulation of dispersed materials, as similarly discussed in a previous report.[34] At higher temperatures of 150˚C and 200˚C the SnO_2 films began to exhibit features of dried droplets with a rough surface (Figure S1), indicating that the deposition process had transitioned from the wet spray regime to the dry regime as illustrated in previous reports.[29] From detailed characterization by SEM and AFM (Figure 1c-1e), we conclude that the optimal substrate temperature for spraying aqueous SnO_2 is 80˚C. Figure S2 shows the SEM image of the top view of sprayed a-SnO_2 (SnO_2 from aqueous solution).

We also optimized the precursor flow rate in the range 40 - 60 μL/min (see Figure S3) obtaining a smooth and uniform SnO_2 film at 45 μL/min. For flow rates above ~60 uL/min, coffee-ring effects were noticeable. However, even for the optimal films made at 80˚C and 45 μL/min (see Figure 1c-1e), faint non-uniform coffee ring edges were still visible in the film with a roughness of ~25 nm, as measured by AFM and SEM (Figure 1c, Figure 1d and Figure S2).

To further control the capillary flow and reduce the coffee-ring effect, the aqueous SnO_2 dispersion was mixed with a co-solvent of isopropanol and water (optimal volume ratio of v:v=1:1). The isopropanol and water ratio was carefully adjusted to attain a clear and uniform SnO_2 dispersion (Figure S4). It was found that a more homogeneous and uniform SnO_2 film with reduced roughness (~15 nm) was achieved using mixed

solvents (Figure 1b). The resulting microstructure of m-SnO_2 (SnO_2 from mixed solvents) are shown in Figure 1f-1h. The isopropanol addition reduced the surface tension and improved wetting of the precursor solution on ITO. As shown in Figure S7, the average contact angle for SnO_2 aqueous solution on ITO is 67.7°, which is much higher than that for SnO_2 in mixed solvent (16.9°). This result further proves that the mixed solvent is favorable to increase the wettability of SnO_2 solution on ITO glass and thus improve the film quality. The mixed solvent system can also prevent the pinning of the drop contact line and suppresses the formation of coffee rings. A similar effect has been observed previously in the case of ZnO.[35] The uniform and full coverage SnO_2 films with mixed solvents was expected to improve solar cell performance.

2. SnO_2 nanocomposite strategy

The optimal thickness of SnO_2 ETL films varies from a few nm to tens of nm and the interface with the perovskite layer is important for managing charge dynamics,[36] stability,[37] and hysteresis.[38] The SnO_2 film morphology and density are also important together with the control of pinholes. To reduce and mitigate any pinhole defects present in sprayed SnO_2 nanoparticle films, we developed a strategy using a bilayer SnO_2/SnO_x nanocomposite (bi-SnO_2) where voids in SnO_2 nanoparticle films were infiltrated with a sprayed sol-gel $SnCl_2$. Specifically, $SnCl_2$ dissolved in isopropanol with different concentrations was sprayed on top of m-SnO_2 layers at a low temperature of 100˚C. After deposition, the SnO_2 nanocomposite film was treated with UV-Ozone for 10 minutes in order to complete sol-gel conversion with accelerated condensation reactions [39] and improved perovskite wetting of the SnO_2 nanocomposite thin film.

The morphology of the SnO_2 composite is shown in Figure 2a and Figure S8. SnO_2 nanoparticle films are observed to be filled with SnO_x from the $SnCl_2$ deposition which infiltrated the voids/gaps and passivated the pinholes in the m-SnO_2. More details about $SnCl_2$ passivation effects will be discussed later. Importantly, the entire spray coating process of the bilayer SnO_2 composite was completed at a low temperature (⩽100˚ C). As similarly observed in a previous report, ultrasonic energy can accelerate the surface

evaporation of liquid molecules, and as a result the shrinkage and sintering of film occurs at relatively low temperature.[40]

X-ray diffraction (XRD) was performed to identify the crystalline phase composition of the m-SnO_2 and bi-SnO_2 composite are shown in Figure 3b. The diffraction peaks of m-SnO_2 clearly match the main characteristic peaks for rutile SnO_2 with high crystallinity.[41] Comparably, XRD of SnO_x from sprayed $SnCl_2$ shows a broad hump corresponding to the glass substrate and amorphous film structure. The optimal combination of highly crystalline SnO_2 nanoparticles and amorphous SnO_x is the key to maintain high electron conductivity and high hole blocking effects.

XPS was used to further analyze the composition of the sprayed SnO_x before and after UV-Ozone treatment. The full XPS spectrum in Figure S9 shows the presence of Sn and O with greatly decreased residual Cl for films after UV-Ozone treatment, revealing that UV-Ozone environment is favorable for $SnCl_2$ conversion to SnOx, as reported elsewhere.[28] Meanwhile, residual Cl on SnO_x after the 10 min UV-Ozone treatment was found to be important for interface optimization and beneficial for increasing V_{oc}, which will be discussed later.[42]

We investigated the compactness of SnO_2 ETL using an electrochemical cyclic voltammetry method to quantify the pinhole or defect density in the SnO_2 layer.[37] Specifically, the sprayed SnO_2 film on ITO was used as a working electrode, and active redox species in the electrolyte were used to monitor the electron transfer rate at the ITO/SnO_2 interface by measuring the current flow when applying bias potentials (Figure 2c). Typical oxidation-reduction peaks were observed for the bare ITO substrate showing a fast and efficient redox reaction occurring at the ITO/solution interface. In comparison, the current decreased by over 50 times (Figure 2c) for the SnO_2 nanocomposite coated ITO indicating that the high compactness of the SnO_2 layer sufficiently blocks interfacial charge transfer.

We also studied the quality of a-SnO_2 and m-SnO_2 with the same method, showing that m-SnO_2 has a higher blocking effect than a-SnO_2, which can further explain the higher

V_{oc} and PCEs for m-SnO_2 based devices compared to a-SnO_2 (Table S2). These results demonstrate that the bi-SnO_2 nanocomposite strategy with enhanced compactness is beneficial in managing charge transfer at the ITO/ETL interface.

3. Solar cell performance

SnO_2 nanoparticle layers: ETL thickness is a key parameter to balance charge transfer and recombination kinetics at the ETL/perovskite interface in solar cells. The ETL needs to be thin enough to have low resistance while highly compact to reduce recombination losses. Therefore, we studied the effects of SnO_2 thickness by controlling the number of aqueous SnO_2 precursor spray passes. An average deposition rate of about 5–7 nm/pass was measured, as the SnO_2 layer increased from 14 nm (2 passes) to 50 nm (10 passes), as shown in Figure 3a.

a-SnO_2 ETLs with varied thickness were used in planar n-i-p solar cells (see inset image in Figure 3c). a-SnO_2 layers with 8 spray passes showed the best performance in PSCs with a champion PCE over 13% (Figure 3b). Detailed photovoltaic parameters are shown in Table S1. The low PCEs for the devices with fewer spray passes were due to higher density of defects (e.g. pinholes), and with increasing to 10 spray passes, the roughness of the SnO_2 films (Figure S5) increased, which may be the reason for the low repeatability of devices (large variation in efficiencies as shown in Figure 3a).

As observed from the microstructure of sprayed films (Figure 1), the solvent system for the SnO_2 precursor plays an important role in the film quality and we compared two types of SnO_2 ETL, a-SnO_2 and m-SnO_2, based on the optimal thickness. Figure 3c displays current density-voltage (*J-V*) curves of champion devices. The devices with m-SnO_2 exhibited a maximum PCE of 15.9% with V_{oc} (1055 mV) and fill factor (FF) (0.72), an improvement compared to a-SnO_2 (PCE=13.1%, V_{oc}=957 mV, FF=0.62). The significantly enhanced photovoltaic parameters for m-SnO_2, especially V_{oc}, was largely due to a more uniform ETL layer (Figure 1) with a higher recombination resistance and fewer charge losses. The difference in hole blocking effects for the two types of SnO_2 will be discussed later. Figure 3c displays the PCE

histogram of devices with a-SnO_2 and m-SnO_2, showing remarkable improvement in PCE when using mixed solvents compared to aqueous processing.

SnO_2/SnOx nanocomposite: To evaluate the bilayer strategy, bi-SnO_2 made with different concentrations of $SnCl_2$ (5-20 mM) were studied in solar cells with their device *J-V* curves shown in Figure 4a. Significant enhancement of V_{oc} (over 100 mV) was achieved for the bi-SnO_2 compared to a-SnO_2 films, demonstrating that the nanocomposite structure greatly reduces the defect density and blocks interfacial recombination. As shown in the Figure S9, there are pinholes as defects in SnO_2 nanoparticle films, which enables perovskite formation in the voids of SnO_2 film. In the working condition, some of the electrons are injected into and transported through SnO_2 nanoparticles, but the electrons collected in FTO can be also transferred back to perovskite, which increases the charge recombination in perovskite film. In the case of SnO_2/SnOx composite, amorphous SnOx (highlighted in yellow) is filled in the pores/voids of SnO_2 nanoparticle film, which can effectively prevent the contact between perovskite and ITO glass. The electrons can be quickly injected into and transported through SnO_2 nanoparticles (high conductivity), but the electron back transfer is efficiently blocked by amorphous SnOx (low conductivity and suitable energy alignment), and therefore the charge recombination is greatly suppressed. This agrees well with the electrochemical measurements in Figure 2c and the high Voc obtained in devices based on SnO_2/SnOx in Figure 3. Similarly, Lin and coworkers found amorphous TiO_2 buffer layer positioned at the interface of anatase TiO_2 effectively improves the electron diffusion and transport, leading to enhanced Jsc and PCE.[43] In addition, we found that when the $SnCl_2$ concentration increased from 5 mM to 10 mM, both J_{sc} and V_{oc} increased. This may be attributed to the chlorine (Cl) remaining in the SnO_2 nanocomposite (Figure S10) which provides a "Cl-passivation" effect to suppresses the interfacial recombination, described previously.[41] However, these photovoltaic parameters, especially FF and J_{sc}, declined when the $SnCl_2$ concentration increased to 20 mM, suggesting that the top SnO_x layer from $SnCl_2$ increases the series resistance (Rs) of ETLs. Figure S11a shows the I-V curves of

ITO/ETL/Ag (ETL: a-SnO_2, m-SnO_2 and bi-SnO_2). It's seen that a-SnO_2 and m-SnO_2 have similar charge conductivities, which is slightly higher that for bi-SnO_2. This could be due to the low conductivity of amorphous SnOx in bi-SnO_2. In order to further study the charge conducting property, the series resistance (Rs) of the devices was analyzed, as shown in Figure S11b. The devices with bi-SnO_2 have lower Rs (about 35 ohm) than a-SnO_2 (about 50 ohm) and m-SnO_2 (about 50 ohm), which could be related to the fact that the presence of chlorine in bi-SnO_2 can passivate the trap sites at the SnO_2/perovskite interface, which leads to efficient interfacial charge transfer and reduced charge recombination for bi-SnO_2, as similarly observed in previous work.[44] Figure S12 shows the transmittance of three types of SnO_2 ETLs, which illustrate that all three SnO_2 have similarly high transmittance in order to guarantee the high light absorption capacity in devices. Figure S13 shows steady-state photoluminescence (PL) and time-resolved photoluminescence (TRPL) characterizations for perovskite films based on a-SnO_2, m-SnO_2, and bi-SnO_2 ETL. As seen from PL spectra in Figure S13a, the devices with three types of SnO_2 ETL show similar PL intensities, which are much lower than perovskite film, demonstrating efficient charge transfer processes at interfaces. Figure S13b exhibits the TRPL to illustrate the charge dynamics at interfaces. The decay curves were fitted to a bi-exponential form where the fast time constant τ_1 corresponds to monomolecular surface recombination and the slow time constant τ_2 corresponds to bimolecular bulk recombination. The device based on bi-SnO_2 shows the shortest PL decay time compared with those of a-SnO_2 and m-SnO_2, further proving faster electron transfer between perovskite and bi-SnO_2.

Figure 4b shows the maximum power point tracking (MPP) of the device based on bi-SnO_2 (10mM $SnCl_2$). The photovoltaic parameters, including V_{oc}, J_{sc} and PCE all retain over 95 % of initial values after 1000 s in ambient condition (relative humidity of 50%, unencapsulated devices under full spectrum one-sun illumination), indicating stabilized power outputs of bi-SnO_2 based PSC devices.

4. Scalable deposition of SnO_2 for large area devices

We first applied sprayed SnO_2 bilayer nanocomposites in fabricating larger 1 cm^2 active area perovskite solar cells on 2x2 cm^2 substrates (inset image in Figure 4d). Figure 4c shows the J-V curves of 1cm^2 devices based on bi-SnO_2 with forward (from J_{sc} to V_{oc}) and backward (from V_{oc} to J_{sc}) scans. The champion device shows a promising PCE of 16.0% (V_{oc}=1093 mV, J_{sc}=22.2 $mAcm^{-2}$, FF=0.66) at backward scan and 16.1% at forward scan (V_{oc} =1094 mV, J_{sc} =22.0 $mAcm^{-2}$, and FF =0.67) indicating a negligible hysteresis in the device, further demonstrating that a Cl-passivated SnO_2/perovskite interface improves charge transfer, as similarly found in previous reports.[41] The inset image in Figure 4c displays the MPP stability of the unsealed large-area device for 3000 seconds in ambient condition with a relative humidity of 50%, showing that the device maintains over 95% of initial performance. We also monitored the long-term stability of unsealed solar cells stored in a N_2-filled glovebox, and the devices maintain about 90% of their initial PCE after 3 months, indicating that spray coated bi-SnO_2 is promising for use in both efficient and stable planar PSCs.

To further evaluate the sprayed SnO_2 nanocomposite for scalable PSCs, a large area substrate (5 cm x 5 cm) was coated with bi-SnO_2 and used to fabricate solar modules (Figure S14a). The module was composed of 6 individual cells with a total active area of 2.1 cm^2 (0.35 cm^2 active area for each cell). The modules were formed by monolithically interconnecting the 6 individual cells in series (Figure S14b). It should be noted that the aim of making solar modules was to demonstrate the scalability of sprayed SnO_2, rather than optimizing for high efficiency since the perovskite was spin-coated. Previous devices made with spin-coated perovskite on NiO were shown to have a significant increase in series resistance and lower performance due to the difficulty of scaling the perovskite layer to 25 cm^2 substrates (Figure S15). The edge effects of spin-coating become more apparent when moving to larger substrates. *J-V* curves of the solar modules are displayed in Figure S14b, showing a high V_{oc} of 6.1 V (more than 1.0 V for each cell in average).

The high voltage of obtained in the solar modules suggests that the bottom SnO_2 ETL has good uniformity, homogeneity and compactness, enabling efficient reduction of the

interfacial charge losses by recombination and few pinholes since shunting was not observed. Additionally, the devices show little *J-V* hysteresis, which is important for operational stability. Unencapsulated modules exhibited good MPP stability by retaining over 95% of initial PCE after 1000 s in ambient conditions with a high relative humidity of 50% (see Figure S14c). The high photovoltaic performance as well as good stability of bi-SnO_2 based solar modules indicates the great potential of using bi-SnO_2 in future large-area PSCs or modules.

Conclusion

In this work, we used an ultrasonic spray coating for SnO_2 ETL scalable deposition in efficient planar perovskite solar cells. The spray deposition of SnO_2 is cost-effective (material usage: 1 wt% μL cm^{-2}), fast (20 s/cm^2), and done in under low-temperature ($\leqslant 100^{\circ}$ C) and open-air conditions which are highly compatible with large area industrial fabrication. We systematically optimized the experimental parameters in the spray coating process and found that a mixed solvent system (volume ratio of H_2O : IPA=1:1) deposited on a heated substrate at 80°C is crucial for reducing the coffee-ring effects in SnO_2 thin films. To further improve the morphology and uniformity of SnO_2 ETL for planar PSCs, we developed a high-quality bilayer SnO_2 nanocomposite by covering crystalline SnO_2 nanoparticles with amorphous SnO_x from $SnCl_2$. Detailed electrochemical and structural characterization demonstrated that this bilayer strategy can sufficiently maintain high electronic conductivity as well as increasing hole blocking to achieve high PCE of over 18 % (active area=0.2 cm^2) and over 16 % (active area=1 cm^2) in planar PSCs with the SnO_2 nanocomposite. More importantly, solar cells incorporating the SnO_2 nanocomposite show little current-voltage hysteresis and remarkable shelf-life stability by maintaining over 90 % of initial performance after 2500 hours storage. We also fabricated large area solar cell devices and solar modules (6 cells series-connected) based on bi-SnO_2. A high V_{oc} over 6.0 V as well as good operational stability was achieved for solar cell modules. We believe that this scalable spray coating of high-quality SnO_2 is promising for future application in large scale production of perovskite solar cells.

Author Contributions

Conceptualization and manuscript writing by J.Z. Investigation, methodology, and formal analysis by J.Z., Y.D., G.J., A.C.F., Z.P., W.J.S., O.Z., J.P.C., L.Y., and N.R. Project administration, funding acquisition, manuscript review, and supervision by R.H.D.

Conflict of Interest

There are no conflicts to declare.

Acknowledgements

This work was supported by the U.S. Department of Energy's Office of Energy Efficiency and Renewable Energy (EERE) under Solar Energy Technologies Office (SETO) Agreement Number DE-EE0008559. Part of this work was performed at the Stanford Nano Shared Facilities (SNSF), supported by the National Science Foundation under award ECCS-1542152. J. Zhang gratefully acknowledges the Wallenberg foundation for a postdoc fellowship, research support by Fundamental Research Funds for the Central Universities (No. 20720200075), Guangdong International Cooperation Project (No.2019A050510002) and Guangdong Basic and Applied Basic Research Foundation (2020A1515110068). Additional support was provided by the National Science Foundation Graduate Research Fellowship, awarded to O. Zhao, J. Chen, and N. Rolston under award DGE-1656518.

Reference

1. Z. Shi and A. H. Jayatissa, *Materials (Basel)*, 2018, **11**,729.
2. L. Wang, H. Zhou, J. Hu, B. Huang, M. Sun, B. Dong, G. Zheng, Y. Huang, Y. Chen and L. Li, *Science*, 2019, **363**, 265–270.
3. J. Correa-Baena, Y. Luo, T. M. Brenner, J. Snaider, S. Sun, X. Li, M. A. Jensen, N. T. P. Hartono, L. Nienhaus, S. Wieghold, J. R. Poindexter, S. Wang, Y. S. Meng, T. Wang, B. Lai, M. V. Holt, Z. Cai, M. G. Bawendi, L. Huang and D. P. Fenning, *Science*, 2019, **363**, 627-631.
4. P. Cui, D. Wei, J. Ji, H. Huang, E. Jia, S. Dou, T. Wang, W. Wang and M. Li, *Nature Energy*, 2019, **4**, 150-159.
5. F. Wang, Y. Cao, C. Chen, Q. Chen, X. Wu, X. Li, T. Qin and W. Huang, *Advanced Functional Materials*, 2018, **28**,1803753.
6. Y. Zheng, J. Kong, D. Huang, W. Shi, L. McMillon-Brown, H. E. Katz, J. Yu and A. D. Taylor, *Nanoscale*, 2018, **10**, 11342-11348.
7. F. Hilt, M. Q. Hovish, N. Rolston, K. Brüning, C. J. Tassone and R. H. Dauskardt, *Energy & Environmental Science*, 2018, **11**, 2102-2113.
8. X. Li , D. Bi , C. Yi , J. D. Decoppet , J. Luo , S. M. Zakeeruddin , A. Hagfeldt and M. Gratzel, *Science*, 2016, **353** , 58-62
9. J. E. Bishop, T. J. Routledge and D. G. Lidzey, *J. Phys. Chem. Lett.*, 2018, **9**, 1977-1984.
10. Y. Zhong, R. Munir, J. Li, M.-C. Tang, M. R. Niazi, D.-M. Smilgies, K. Zhao and A. Amassian, *ACS Energy Letters*, 2018, **3**, 1078-1085.
11. Y. Galagan, F. Di Giacomo, H. Gorter, G. Kirchner, I. de Vries, R. Andriessen and P. Groen, *Advanced Energy Materials*, 2018, **8**, 1801935.
12. Y. Deng, X. Zheng, Y. Bai, Q. Wang, J. Zhao and J. Huang, *Nature Energy*, 2018, **3**, 560-566.
13. Y. Galagan, *J. Phys. Chem. Lett.*, 2018, **9**, 4326-4335.

14. Y. Chen, L. Zhang, Y. Zhang, H. Gao and H. Yan, *RSC Advances*, 2018, **8**, 10489-10508.

15. J. Zhang, B. Xu, M. B. Johansson, M. Hadadian, J. P. Correa Baena, P. Liu, Y. Hua, N. Vlachopoulos, E. M. J. Johansson, G. Boschloo, L. Sun and A. Hagfeldt, *Advanced Energy Materials*, 2016, **6**, 1502536.

16. J. Zhang, B. Xu, L. Yang, A. Mingorance, C. Ruan, Y. Hua, L. Wang, N. Vlachopoulos, M. Lira-Cantú, G. Boschloo, A. Hagfeldt, L. Sun and E. M. J. Johansson, *Advanced Energy Materials*, 2017, **7**, 1602736.

17. M. C. Jung, S. R. Raga, L. K. Ono and Y. Qi, *Sci. Rep.*, 2015, **5**, 9863.

18. T. Bu, J. Li, F. Zheng, W. Chen, X. Wen, Z. Ku, Y. Peng, J. Zhong, Y. B. Cheng and F. Huang, *Nat. Commun*, 2018, **9**, 4609.

19. J. Zhang, B. Xu, M. B. Johansson, N. Vlachopoulos, G. Boschloo, L. Sun, E. M. Johansson and A. Hagfeldt, *ACS Nano*, 2016, **10**, 6816-6825.

20. Q. Jiang, X. Zhang and J. You, *Small*, 2018, **14**, 1801154.

21. J. Luo, Y. Wang and Q. Zhang, *Solar Energy*, 2018, **163**, 289-306.

22. L. Xiong, Y. Guo, J. Wen, H. Liu, G. Yang, P. Qin and G. Fang, *Advanced Functional Materials*, 2018, **28**, 1802757.

23. J. Yang, B. D. Siempelkamp, E. Mosconi, F. De Angelis and T. L. Kelly, Chem. Mater., 2015, **27**, 4229–4236

24. W. Ke, G. Fang, Q. Liu, L. Xiong, P. Qin, H. Tao, J. Wang, H. Lei, B. Li, J. Wan, G. Yang and Y. Yan, *J. Am. Chem. Soc.*, 2015, **137**, 6730-6733.

25. Y. Kuang, V. Zardetto, R. van Gils, S. Karwal, D. Koushik, M. A. Verheijen, L. E. Black, C. Weijtens, S. Veenstra, R. Andriessen, W. M. M. Kessels and M. Creatore, *ACS Appl. Mater. Interfaces*, 2018, **10**, 30367-30378.

26. H. Yi, D. Wang, M. A. Mahmud, F. Haque, M. B. Upama, C. Xu, L. Duan and A. Uddin, *ACS Applied Energy Materials*, 2018, **1**, 6027-6039.

27. L. Qiu, Z. Liu, L. K. Ono, Y. Jiang, D. Y. Son, Z. Hawash, S. He and Y. Qi, *Advanced Functional Materials*, 2018, **29**, 1806779

28. L. Huang, X. Sun, C. Li, J. Xu, R. Xu, Y. Du, J. Ni, H. Cai, J. Li, Z. Hu and J. Zhang, *ACS Appl. Mater. Interfaces*, 2017, **9**, 21909-21920.

29. S. Bose, S. S. Keller, T. S. Alstrom, A. Boisen and K. Almdal, *Langmuir*, 2013, **29**, 6911-6919.

30. N. Rolston, A. D. Printz, F. Hilt, M. Q. Hovish, K. Brüning, C. J. Tassone and R. H. Dauskardt, *Journal of Materials Chemistry A*, 2017, **5**, 22975-22983.

31. W. J. Scheideler, N. Rolston, O. Zhao, J. Zhang and R. H. Dauskardt, *Advanced Energy Materials*, 2019, **9**, 1803600.

32. Y. Li, Q. Yang, M. Li and Y. Song, *Sci Rep*, 2016, **6**, 24628.

33. D. Soltman and V. Subramanian, *Langmuir*, 2008, **24**, 2224-2231.

34. J. Qi, S. Chen, C. Lan, A. C. Wang, X. Cui, Z. You, Q. Zhang, Y. Li, Z. Wang, H. Wang, Z. Lin, *Advanced Energy Materials*, 2020, **10**, 2001185.

35. C. Jiang, Z. Zhong, B. Liu, Z. He, J. Zou, L. Wang, J. Wang, J. Peng and Y. Cao, *ACS Appl. Mater. Interfaces*, 2016, **8**, 26162-26168.

36. J. Zhang, Q. Daniel, T. Zhang, X. Wen, B. Xu, L. Sun, U. Bach and Y. B. Cheng, *ACS Nano*, 2018, **12**, 10452-10462.

37. J. Zhang, A. Hultqvist, T. Zhang, L. Jiang, C. Ruan, L. Yang, Y. Cheng, M. Edoff and E. M. J. Johansson, *ChemSusChem*, 2017, **10**, 3810-3817.

38. J. Zhang, T. Zhang, L. Jiang, U. Bach and Y.-B. Cheng, *ACS Energy Letters*, 2018, **3**, 1677-1682.

39. W. J. Scheideler, M. W. McPhail, R. Kumar, J. Smith and V. Subramanian, *ACS Appl Mater Interfaces*, 2018, **10**, 37277-37286.

40. X. Zhang, F. Zabihi, H. Xiong, M. Eslamian, C. Hou, M. Zhu, H. Wang and Q. Zhang, *Chemical Engineering Journal*, 2020, **394**, 124887.

41. W. Chen, Q. Zhou, F. Wan and T. Gao, *Journal of Nanomaterials*, 2012, **2012**, 1-9.

42. H. Tan, A. Jain, O. Voznyy, X. Lan, F.P. G. De Arquer, J. Z. Fan, R. Quintero-Bermudez, M. Yuan, B. Zhang, Y. Zhao, F. Fan, P. Li, L. Quan, Y. Zhao, Z. Lu, Z. Yang, S. Hoogland and E. H. Sargent, *Science*, 2017, **355**, 722-726.

43. B. Wang, M. Zhang, X. Cui, Z. Wang, M. Rager, Y. Yang, Z. Zou, Z. L. Wang and Z. Lin, *Angew Chem Int Ed Engl*, 2020, **59**, 1611-1618.

44. E. Mosconi, E. Ronca and F. De Angelis, *J Phys Chem Lett*, 2014, **5**, 2619-2625.

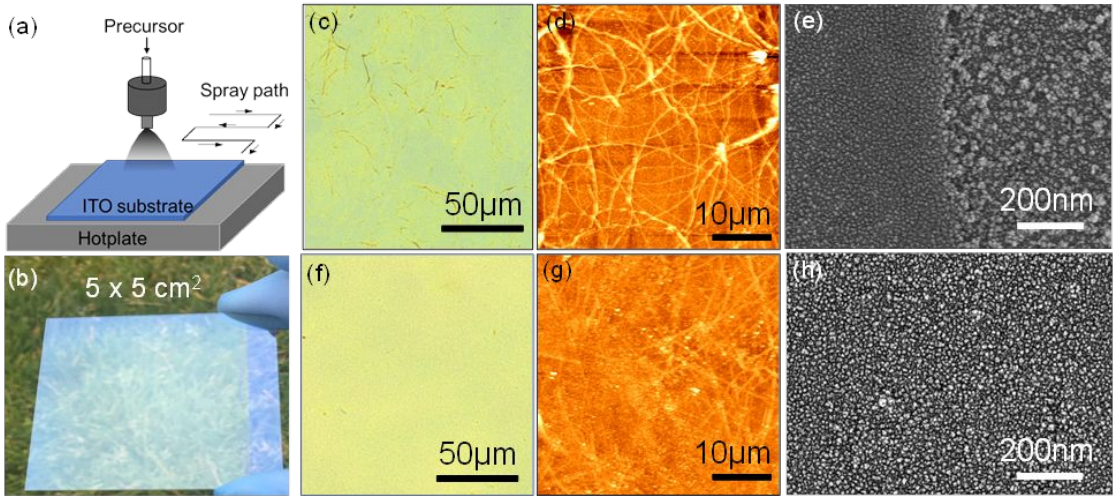

Figure 1. Spray deposition system and microstructure of sprayed SnO_2 films. (a) Schematic of ultrasonic spray deposition system with N_2 as carrier gas, the spray speed is 25 mm/s and the pass spacing is 2 mm. (b) image of SnO_2 thin film on 5x5 cm^2 ITO substrate (no SnO_2 layer on the right side of ITO substrate for comparation). Microstructure characterization of sprayed a-SnO_2 (c, d, e) and m-SnO_2 (f, g, h) by microscope (c and f), atomic force microscopy (AFM) (d and g) and scanning electron microscopy (SEM) (e and h), respectively. (a-SnO_2: SnO_2 from aqueous solution; m-SnO_2: SnO_2 from mixed solution).

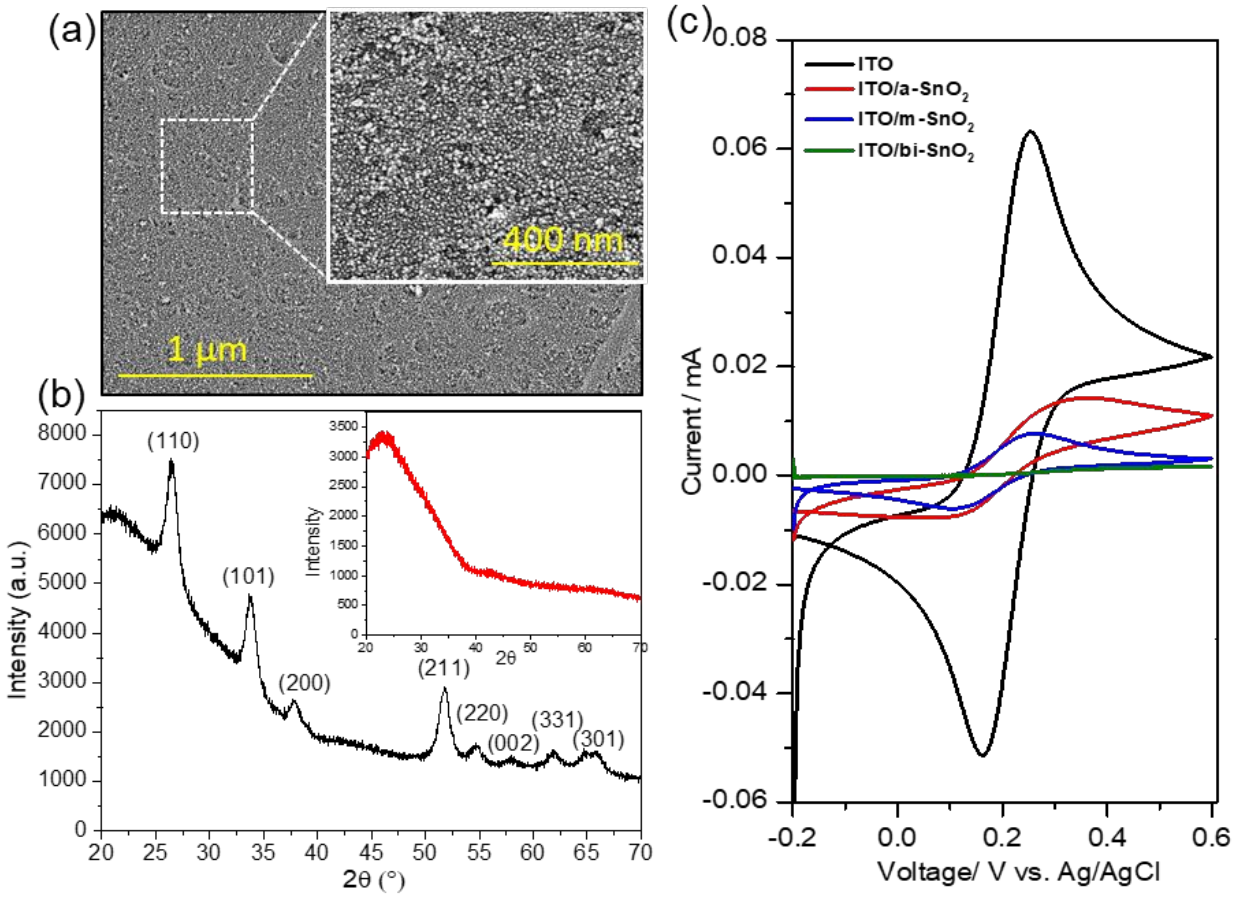

Figure 2. (a) SEM image (top view) of *bi*-SnO_2 layer on ITO substrate. (b) XRD images of the m-SnO_2 (black curve) and SnO_x from $SnCl_2$ (red curve in inset image). (c) Cyclic voltammetry curves of $K_4Fe(CN)_6$ in aqueous solution with ITO, ITO/a-SnO_2, ITO/m-SnO_2 and ITO/*bi*-SnO_2 as working electrodes.

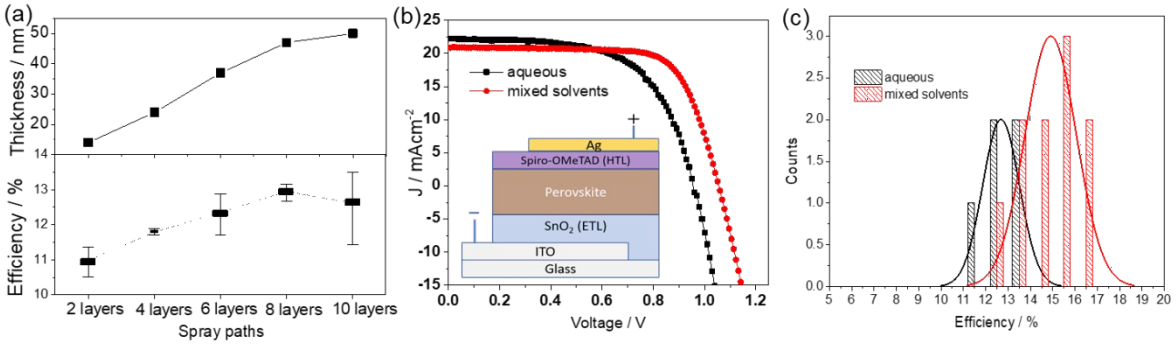

Figure 3. (a) Thickness dependence of a-SnO_2 vs. number of spray passes from 0 to 10 layers (up) and PCE distribution of the solar cells based on a-SnO_2 with different thicknesses (down). (b) *J-V* curves of the champion devices based on a-SnO_2 and m-SnO_2 with 8 spray passes. (c) PCE statistics for devices with a-SnO_2 and m-SnO_2.

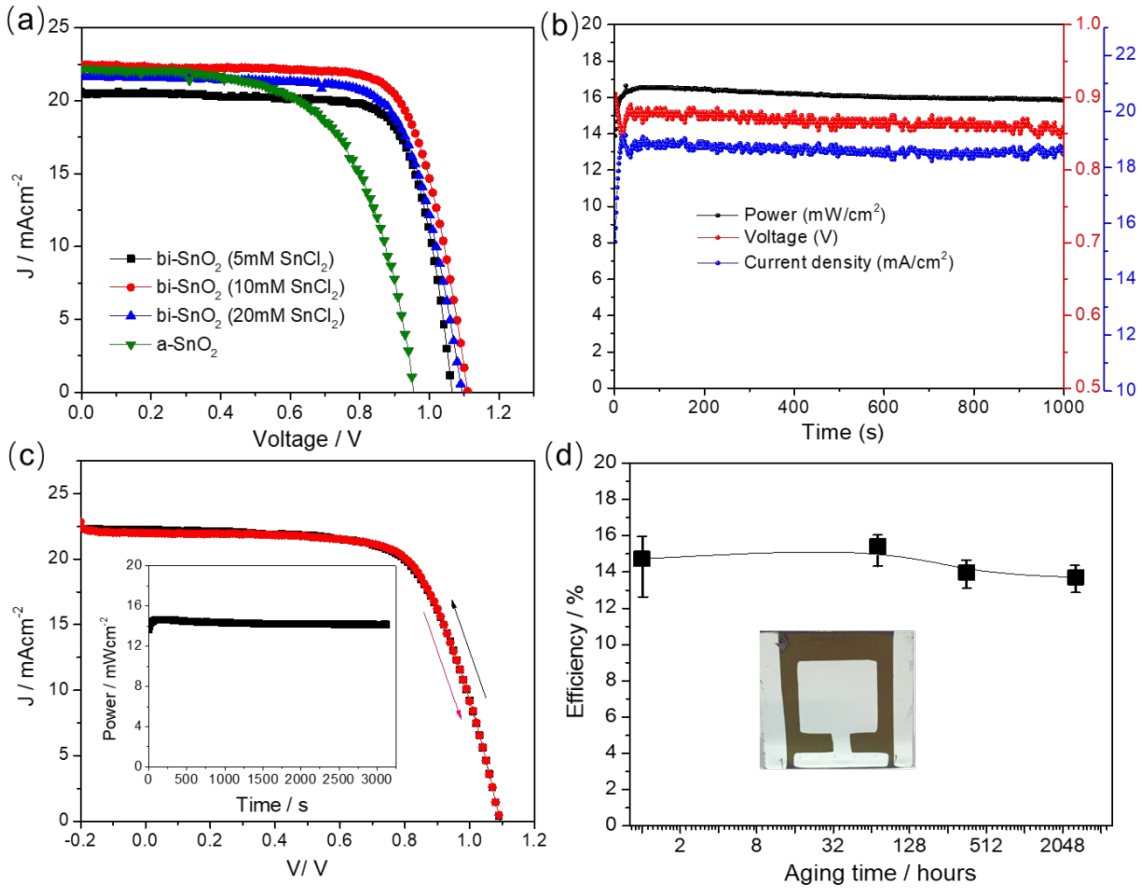

Figure 4. (a) J-V curves of the champion devices based on SnO_2 nanocomposite ($SnCl_2$: 5-20 mM) as ETL and a-SnO_2. (b) Maximum power point tracking of one of the devices based on bi-SnO_2. (c) J-V curves (forward and backward scans) of large area (1cm^2) perovskite solar cells based on bi-SnO_2. Inset image shows the MPP stability of the device. (d) Long term shelf-life of the large-area devices for over 2500 hours. Devices are not encapsulated and stored in N_2-filled glovebox in the dark (O_2 < 100 ppm, H_2O < 10 ppm).